PAPER

Composition-dependent Raman modes of $Mo_{1-x}W_xS_2$ monolayer alloys†

Yanfeng Chen,[a] Dumitru O. Dumcenco,‡[b] Yiming Zhu,[a] Xin Zhang,[c] Nannan Mao,[ad] Qingliang Feng,[ad] Mei Zhang,[a] Jin Zhang,[d] Ping-Heng Tan,[c] Ying-Sheng Huang*[b] and Liming Xie*[a]

Two-dimensional (2D) transition-metal dichalcogenide alloys with tunable band gaps have promising applications in nanoelectronics and optoelectronics. Characterization of structures of 2D alloys, such as composition and atom mixing, is of fundamental importance to their applications. Here, we have conducted systematic Raman spectroscopic studies on $Mo_{1-x}W_xS_2$ monolayers ($0 \leq x \leq 1$). First-order Raman modes and second-order Raman modes have been observed in the range of $100-480$ cm^{-1} in the 2D alloys. The out-of-plane A_1' modes and in-plane E' modes showed one-mode and two-mode behaviors, respectively. The broadening of A_1' and E' modes in the alloys has been observed. The disorder-related Raman peaks at ~ 360 cm^{-1} were only observed in the 2D alloys but not in the two end materials. Modified random-element-isodisplacement (MREI) model has been adopted to successfully predict mode behaviors of A_1' and E' modes in the monolayer alloys. Further, composition-dependent A_1' and E' frequencies can be well fitted by the MREI model, giving composition-dependent force constants.

Introduction

Two dimensional (2D) materials, such as graphene,[1–7] BN[8] and MoS_2,[9–14] have attracted extensive interest in recent years due to their unique structures, fundamental physical properties and potential applications. Layered transition-metal dichalcogenides MX_2 (M = Mo, W, Nb, Ta; X = S, Se, Te), a class of materials of covalently bonded layers stacked together by weak van der Waals forces,[15–18] are a rich source of 2D materials. The direct band-gap nature and hence the emergence of strong photoluminescence (PL) in single layer transition-metal dichalcogenides have made them appealing materials for electronic and optoelectronic devices.[19–22] Band gap engineering of 2D monolayers is important for those applications.[1,23–27] To achieve band gap tuning in 2D monolayers, alloying transition-metal dichalcogenides has been proposed by theoretical calculations[28,29] and demonstrated

in experiments.[30] The key to band gap engineering in monolayer alloys is mixing the end compositions at atomic scale.

Structure characterization of 2D alloys is challenging. Atomic-resolution scanning transmission electron microscopy (STEM) can directly image and discriminate individual atoms.[31] Raman spectroscopy could also be a powerful tool to characterize structures of 2D alloys. For bulk semiconductors, frequency shift was used to determine alloy compositions and peak broadening was used to indicate alloy degree.[32–34] For 2D materials, Raman spectroscopy has been widely used in characterizations of graphene,[4,35–38] MoS_2 (ref. 39–43) and WS_2.[44–47] In this work, we performed a systematic Raman scattering investigation on a series of $Mo_{1-x}W_xS_2$ monolayers. The first-order Raman active A_1' and E' modes and several second-order Raman modes were observed. Polarization dependent Raman scattering measurements were performed to confirm the assignment of A_1', E' and second-order Raman modes in $Mo_{1-x}W_xS_2$ monolayers. In $Mo_{1-x}W_xS_2$ monolayers, the A_1' and E' modes showed one-mode and two-mode behaviors, respectively. The composition-dependent Raman frequency and full width at half maximum (FWHM) of the dominant Raman modes were discussed. Modified random-element-isodisplacement (MREI) model has been used to predict mode behavior and fit frequency shift in the alloys.

[a]CAS Key Laboratory of Standardization and Measurement for Nanotechnology, National Center for Nanoscience and Technology, Beijing 100190, P. R. China. E-mail: xielm@nanoctr.cn; Tel: +86-010 8254 5692

[b]Department of Electronic Engineering, National Taiwan University of Science and Technology, Taipei 106, Taiwan, Republic of China. E-mail: ysh@mail.ntust.edu.tw

[c]State Key Laboratory of Superlattices and Microstructures, Institute of Semiconductors, Chinese Academy of Sciences, Beijing 100083, China

[d]Center for Nanochemistry, College of Chemistry and Molecular Engineering, Peking University, Beijing 100871, China

† Electronic supplementary information (ESI) available: The details of MREI-model calculations. EDX data of $Mo_{1-x}W_xS_2$ alloys. See DOI: 10.1039/c3nr05630a

‡ Current address: Electrical Engineering Institute, Ecole Polytechnique Federale de Lausanne (EPFL), CH-1015 Lausanne, Switzerland.

Experimental section

Sample preparation

$Mo_{1-x}W_xS_2$ single crystals were grown by the chemical vapor transport method.[48,49] 2H-type layered structures and alloy

compositions for all $Mo_{1-x}W_xS_2$ crystals were confirmed by X-ray diffraction (XRD) and energy dispersive X-ray spectroscopy (EDX) (Table S1†), respectively.[48] $Mo_{1-x}W_xS_2$ monolayer samples were mechanically exfoliated on Si/SiO_2 (300 nm SiO_2) substrates from bulk $Mo_{1-x}W_xS_2$ single crystals.

Characterization

The location, shape and layer number of $Mo_{1-x}W_xS_2$ flakes were determined by combination of optical contrast and atomic force microscopy (AFM) imaging as shown in our previous work.[30] Tapping mode AFM was done on a Vecoo IIIa multimode microscope.

Raman and PL measurements were performed on a Renishaw inVia plus under ambient condition at room temperature. The laser excitation was at 514.5 nm (2.41 eV) with a power of ~0.5 mW. The laser spot size was ~1 μm in diameter. The widely used Porto notations $Z(XX)\bar{Z}$ and $Z(XY)\bar{Z}$ have been used for the designation of crystal and polarization directions[50] in this work. In the polarized Raman measurements, for $Z(XX)\bar{Z}$ configuration, a polarization analyzer was placed right after the edge filter and the polarization direction was parallel to the polarization of incident laser beam. The $Z(XY)\bar{Z}$ configuration was conducted by placing a half-wave plate before the analyzer in $Z(XX)\bar{Z}$ configuration.

Results and discussion

$Mo_{1-x}W_xS_2$ monolayer flakes were cleaved from the corresponding bulk single crystals onto SiO_2/Si substrates (oxide thickness of 300 nm). Optical imaging and AFM imaging (Fig. 1a and b) were used to locate and identify $Mo_{1-x}W_xS_2$ monolayers as reported in our previous work.[30] Further, compared with $Mo_{1-x}W_xS_2$ few-layers and bulks, $Mo_{1-x}W_xS_2$ monolayers showed smaller frequency difference between A_1' and E' and much stronger PL emission.[11,30] Fig. 1c shows composition-dependent unpolarized Raman spectra of $Mo_{1-x}W_xS_2$ monolayers with W composition x changing from 0 to 1. Taking Mo and W atom as the same and considering the very small lattice mismatch between two end component MoS_2 (3.15 Å)[51] and WS_2 (3.153 Å),[52] the space group of single layer $Mo_{1-x}W_xS_2$ is expected to be $P\bar{6}m2$ (point group D_{3h}). There are totally 9 normal vibration modes at the Γ point in the Brillouin zone for MoS_2 and WS_2 monolayers,[47,53] in which two accessible first-order Raman active modes can be observed in backscattering experiment[44,54,55] in MoS_2 and WS_2 monolayers: A_1' and E'. The atomic displacements of Raman modes A_1' and E' are shown in Fig. 1d. The A_1' mode is an out-of-plane vibration involving only the S atoms while the E' mode associates to in-plane displacement of transition metal Mo or W and S atoms.

Similar to that of $Mo_{1-x}W_xS_2$ bulk alloys,[48,49] A_1' and E' modes of $Mo_{1-x}W_xS_2$ monolayer alloys showed one-mode and two-mode behaviors, respectively. That is, A_1' mode shifts continuously as the W composition x. While two phonon branches associated to E' modes of MoS_2 and WS_2 are observed in alloys. As the composition of W increases, the relative intensity of WS_2-like E' mode increases, while that of the MoS_2-
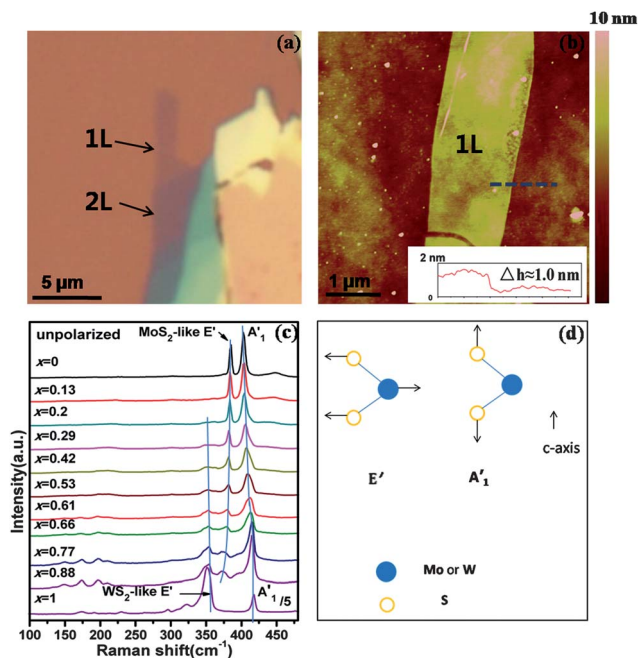

Fig. 1 (a) Optical micrograph of exfoliated $Mo_{0.47}W_{0.53}S_2$ flake deposited on the 300 nm SiO_2/Si substrate. Monolayer and bilayer regions are indicated by arrows and marked by "1L"and "2L", respectively. (b) AFM image of the $Mo_{0.47}W_{0.53}S_2$ monolayer (1L) in panel (a). The inset shows the height profile along the blue dashed line. (c) Raman spectra of $Mo_{1-x}W_xS_2$ monolayers with different W composition x. The three solid (blue) lines guided by eyes show frequency shift of E' and A_1' peaks with W composition x. (d) The schematics of displacement of atoms for the Raman active E' and A_1' modes in $Mo_{1-x}W_xS_2$ monolayer.

like E' mode decreases. The intensities of A_1' and E' modes of WS_2 monolayer is much stronger than that of other $Mo_{1-x}W_xS_2$ samples (Fig. 1c) due to the resonance enhancement (B exciton energy of WS_2 centered at ~2.36 eV (ref. 30)).

In order to confirm the assignments of A_1', E' modes as well as the second-order Raman features in $Mo_{1-x}W_xS_2$ monolayer alloys, polarization-dependent backscattering experiments have been carried out. For D_{3h} point group, the corresponding polarizability tensors of the above two first-order Raman modes A_1' and E' are:[56]

$$\alpha\left(A_1'\right) = \begin{bmatrix} a & 0 & 0 \\ 0 & a & 0 \\ 0 & 0 & b \end{bmatrix},$$
$$\alpha\left(E_1'\right) = \begin{bmatrix} 0 & d & 0 \\ d & 0 & 0 \\ 0 & 0 & 0 \end{bmatrix}, \begin{bmatrix} d & 0 & 0 \\ 0 & -d & 0 \\ 0 & 0 & 0 \end{bmatrix} \quad (1)$$

Based on polarizability tensor, A_1' mode should be observed only under $Z(XX)\bar{Z}$ configurations, but not in $Z(XY)\bar{Z}$ configurations. E' mode should be present under both $Z(XX)\bar{Z}$ and $Z(XY)\bar{Z}$ configurations. The Raman peak around 400–420 cm^{-1} (Fig. 2) presented only at $Z(XX)\bar{Z}$ configuration was confirmed to be A_1'. The Raman peaks at ~380 cm^{-1} and 350 cm^{-1} (Fig. 2) presented both under $Z(XX)\bar{Z}$ and $Z(XY)\bar{Z}$ configurations were confirmed to be MoS_2-like and WS_2-like E' modes, respectively.

Note that, for WS$_2$ monolayer, the lower lying Raman band at ~350 cm^{-1} consists of two components (Z(XY)$\bar{Z}$ configuration in Fig. 2f): one is assigned to E' mode at ~355 cm^{-1}, and the other is assigned to 2LA(M) at ~350 cm^{-1}.[44] In addition, the intensity of 2LA(M) mode in both unpolarized (Fig. 1c for $x = 1$) and Z(XX)$\bar{Z}$ (Fig. 2f) configurations is the strongest one due to a double-resonant Raman process[44] and dramatically decreases in Z(XY)$\bar{Z}$ configuration (Fig. 2f). The other second-order (SOR) modes (at 263, 295 and 323 cm^{-1}) can be attributed to the combinations of phonons at M point.[44,57] The Raman peak at 323 cm^{-1} is weaker in Z(XY)$\bar{Z}$ configuration than that in Z(XX)$\bar{Z}$ configuration, while the peaks at 263 and 295 cm^{-1} disappear in Z(XY)$\bar{Z}$ configuration.

For Mo$_{1-x}$W$_x$S$_2$ monolayer alloys with $x = 0$, 0.20 and 0.42 (Fig. 2a–c), the asymmetric broad Raman peak at ~450 cm^{-1} can be assigned to the overlap of a longitudinal acoustic mode 2LA(M) and a normally Raman inactive A$_2''$ optical mode.[43] In addition, the intensity of the Raman peak at ~450 cm^{-1} decreases obviously in the corresponding Z(XY)$\bar{Z}$ configuration. For Mo$_{1-x}$W$_x$S$_2$ monolayer alloys with $x = 0.20$, 0.42, 0.61 and 0.77 (Fig. 2b–e), detailed multi-peak curve fittings (as shown in the Fig. 2b–e insets) are performed and the assignment of peaks can be carried out by comparing the locations and polarization dependence with that of the constituent end samples MoS$_2$ and WS$_2$.[43,44] The Raman peak at ~360 cm^{-1} appearing from $x = 0.13$ to $x = 0.77$ was assigned to an alloy disorder-related peak.[49,58]

Fig. 3a shows the composition-dependent Raman frequencies of the different Raman modes in Mo$_{1-x}$W$_x$S$_2$ monolayer alloys. With the increasing of W composition, MoS$_2$-like E' peak shifts to lower frequency, while WS$_2$-like E' peak moves slowly towards higher frequency. The A$_1'$ modes upshift with increasing W composition in monolayer alloys. These variation trends of Raman frequencies are similar to that of Mo$_{1-x}$W$_x$S$_2$ bulk alloys (Fig. 4b).[49] The peak frequency of disorder-related mode at ~360 cm^{-1} is not sensitive to alloy composition. The peak frequency at ~346 cm^{-1} (2LA(M) of WS$_2$) overall shows a decrease trend with decreasing W composition.

Since the monolayer alloys have random distributions of Mo and W atoms without phase separation throughout all W contents.[31] Mo, W or S atoms should have several different nearest Mo and W coordination configurations in Mo$_{1-x}$W$_x$S$_2$ monolayer alloys. This can introduce reduced mass and force constant fluctuation,[32–34] which is responsible for the asymmetric line shapes and peak broadening (see Fig. 1c). The variations of FWHM of the first-order Raman active modes are depicted in Fig. 3b and c.

The FWHM of A$_1'$ mode increases from ~6.2 cm^{-1} (at $x = 0$) to ~12.9 cm^{-1} (at $x = 0.61$) and then decreases to ~5.7 cm^{-1} at $x = 1$ (Fig. 3b). The maximum peak width at intermediate W compositions may indicate disorder-induced broadening. For E' modes (see Fig. 3c), as the W composition increases, the FWHM of WS$_2$-like E' increases first from ~10.8 cm^{-1} (at $x = 0.20$) to ~13.7 cm^{-1} (at $x = 0.42$), then decreases to ~4.8 cm^{-1} at $x = 1$. The FWHM of MoS$_2$-like E' mode almost monotonically increases from ~4 cm^{-1} (at $x = 0$) to ~11.6 cm^{-1} (at $x = 0.88$), instead of reaching a maximum peak width at intermediate W composition. This needs further investigation.

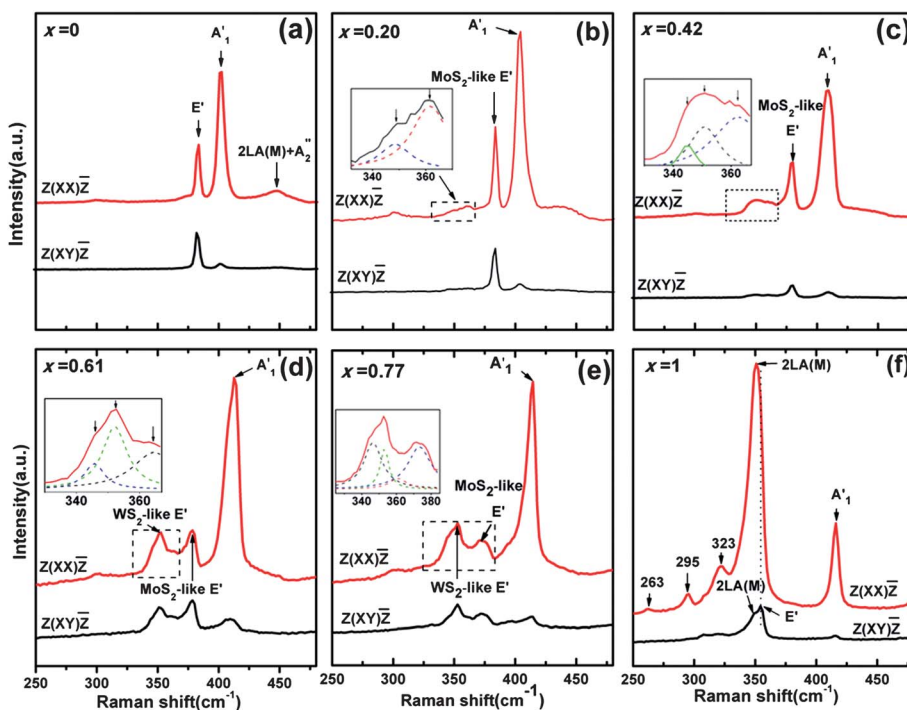**Fig. 2** Polarized Raman spectra of Mo$_{1-x}$W$_x$S$_2$ monolayer alloys in the range 250–480 cm^{-1} in Z(XX)$\bar{Z}$ and Z(XY)$\bar{Z}$ configurations with different W composition x (a) $x = 0$; (b) $x = 0.20$; (c) $x = 0.42$; (d) $x = 0.61$; (e) $x = 0.77$ and (f) $x = 1$. The first-order Raman peaks E', A$_1'$ and several second-order modes are marked by arrows. The insets in (b)–(e) show the detailed line shape fits in the range marked by squares. The solid lines show the experimental curves, while the dashed lines show the fitting results. The arrows in the insets indicate the corresponding fitted peak positions.
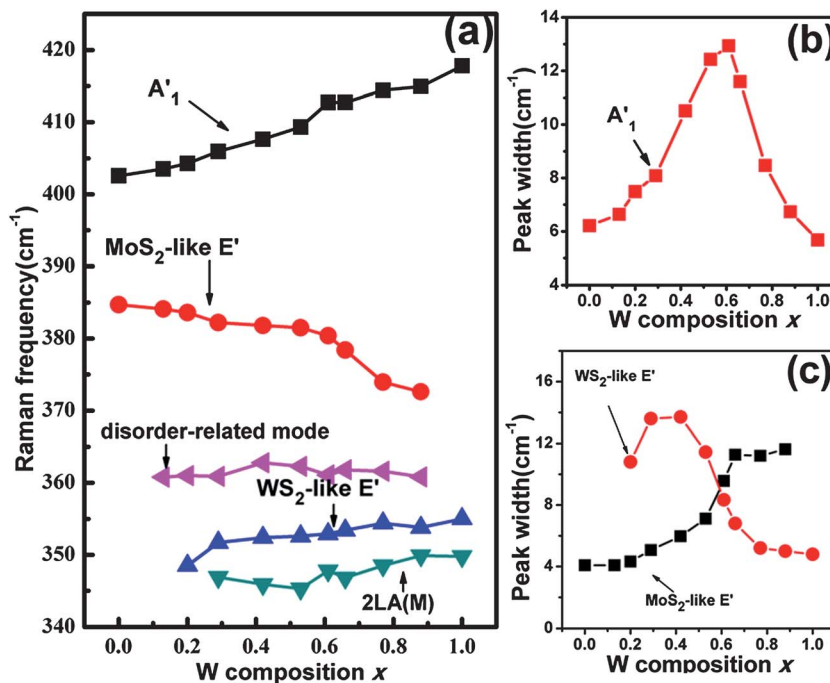
Fig. 3 (a) Composition-dependent Raman frequencies and full width at half maximum (FWHM) of A_1' (b) and E' (c) modes of $Mo_{1-x}W_xS_2$ monolayer alloys.

MREI model has been successfully used to predict and fit lattice vibrational modes of mixed crystal structures, such as $AB_{1-x}C_x$ type[59] and $AB_{2-x}C_x$ type.[60] The MREI model is based on the assumptions of isodisplacement and randomness,[61] *i.e.*, (1) same kind of atoms vibrate in the same amplitude and phase and (2) all substituted atoms are randomly distributed. Previous STEM imaging revealed random distributions of Mo and W atoms, which verifies the 'randomness' assumption.[31] Based on MREI model for $Mo_{1-x}W_xS_2$ monolayer alloys (Fig. 4a), ignoring the S–S interactions, we can write the motion equation for A_1' mode,

$$m_s\ddot{\mu}_s = -(1-x)F_1\mu_s - xF_2\mu_s, \tag{2}$$

where m_s and μ_s are mass and displacement of the S atoms. The terms F_1 and F_2 are force constants representing interactions between S–Mo, S–W along vertical direction, respectively (Fig. 4a). Linear changing of force constants on alloy composition is assumed,

$$\frac{F_1}{F_{10}} = \frac{F_2}{F_{20}} = 1 - \theta_1 x \tag{3}$$

where F_{10} and F_{20} are the limiting values of force constants F_1 and F_2, respectively, as $x \to 0$. The parameter θ_1 takes into account the variation of force constants.

$$\omega^2 = \frac{(1-x)(1-\theta_1 x)F_{10} + x(1-\theta_1 x)F_{20}}{m_s} \tag{4}$$

This predicts one mode behavior for A_1' mode, consistent with experimental observation.
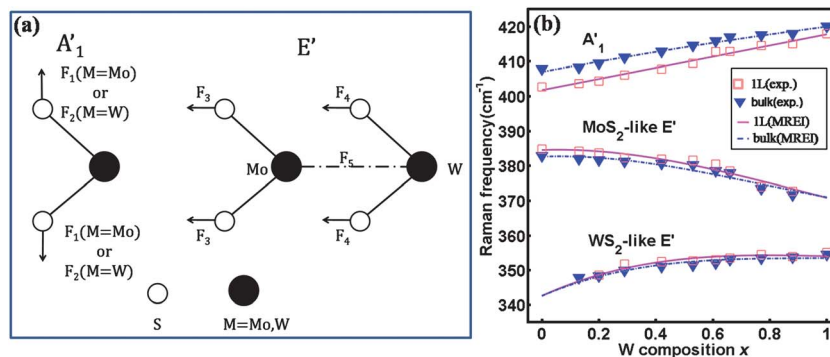

Fig. 4 (a) The schematics of force constants used in MREI model. (b) Composition-dependent Raman frequencies of E' and A_1' (E_{2g}^1 and A_{1g} for bulk) modes in $Mo_{1-x}W_xS_2$ alloys. The solid and dashed lines are the MREI fits of $Mo_{1-x}W_xS_2$ monolayers and bulks, respectively and the scattered square and triangle points are the experimental data of $Mo_{1-x}W_xS_2$ monolayers and bulks.

Table 1 MREI-model parameters for $Mo_{1-x}W_xS_2$ monolayer and bulk alloys (note F is in 10^6 amu cm^{-2})

Fitted parameters	A'_1 (1L) or A_{1g} (bulk)			E'(1L) or E^1_{2g} (bulk)				
	F_{10}	F_{20}	θ_1	F_{30}	F_{40}	F_{50}	θ_2	θ_3
Monolayer alloy	2.581	2.684	−0.040	1.773	2.985	15.615	0.474	−0.101
Bulk alloy	2.649	2.458	−0.148	1.756	2.990	15.610	0.488	−0.115

For E′ mode, the motion equations are

$$m_s\ddot{\mu}_s = -(1-x)F_3(\mu_s - \mu_{Mo}) - xF_4(\mu_s - \mu_W) \quad (5)$$

$$m_{Mo}\ddot{\mu}_{Mo} = -2F_3(\mu_{Mo} - \mu_s) - xF_5(\mu_{Mo} - \mu_W) \quad (6)$$

$$m_W\ddot{\mu}_W = -2F_4(\mu_W - \mu_s) - (1-x)F_5(\mu_W - \mu_{Mo}) \quad (7)$$

where m_s, m_{Mo} and m_W are the mass of S, Mo and W atoms, respectively. μ_s, μ_{Mo} and μ_W are the displacements of S, Mo and W atoms, respectively. F_3, F_4 and F_5 are force constants representing interactions between S–Mo, S–W and Mo–W along horizontal direction, respectively (see Fig. 4a). Instead of linear changing of force constants on alloy composition which gives a poor fitting for experimental E′ data (see Fig. S1†), quadratic changing of force constants is assumed.

$$\frac{F_3}{F_{30}} = \frac{F_4}{F_{40}} = \frac{F_5}{F_{50}} = 1 - \theta_2 x - \theta_3 x^2 \quad (8)$$

where F_{30}, F_{40} and F_{50} are the limiting values of force constants F_3, F_4 and F_5, respectively, as $x \to 0$. The parameters θ_2 and θ_3 take into account the variations of force constants.

Similarly, we can get two eigenvalues (details in ESI†),

$$\omega^2 = \frac{R_1 + R_2 \pm \sqrt{(R_1 - R_2)^2 + 4R_{12}R_{21}}}{2} \quad (9)$$

where

$$R_1 = \frac{(1-x)F_3}{m_s} + \frac{2F_3}{m_{Mo}} + \frac{xF_5}{m_{Mo}}$$

$$R_2 = \frac{xF_4}{m_s} + \frac{2F_4}{m_W} + \frac{(1-x)F_5}{m_W}$$

$$R_{12} = \frac{xF_4}{m_s} - \frac{xF_5}{m_{Mo}}$$

$$R_{21} = \frac{(1-x)F_3}{m_s} - \frac{(1-x)F_5}{m_W}$$

This predicts two-mode behavior for E′ mode, also consistent with experimental observation. If ignoring weak inter-layer interactions in $Mo_{1-x}W_xS_2$ bulk alloys, all formulas used in this model are the same for monolayer alloy and bulk alloy.

The Raman active modes (A_1' and E′ for monolayer, and A_{1g} and E^1_{2g} for bulk) frequency variation with composition is presented in Fig. 4b. The Raman frequency shift is similar for monolayer and bulk alloys. Least square fitting was used to fit the experimental data using eqn (4) and (9). The experimental data can be well fitted, giving similar force parameters for monolayer alloy and bulk alloy (Table 1). Substituting these parameters into eqn (4), for monolayer samples, we can get equation

$$\omega_{A_1'} = 401.6(0.002x^2 + 0.080x + 1)^{1/2}, \quad (10)$$

Meanwhile, substituting these parameters into eqn (9), we can get relationship between frequency and alloy composition for MoS₂-like and WS₂-like E′ modes (see ESI†). The composition-dependent Raman shift can be used to determine the composition in mixed $Mo_{1-x}W_xS_2$ monolayer alloys.

Conclusions

In summary, the Raman spectra of $Mo_{1-x}W_xS_2$ monolayer alloys were studied with W composition x from 0 to 1. The dominant first-order Raman active A_1', E′ and several second-order Raman modes have been observed in the range 100–480 cm^{-1}. A_1' and E′ modes showed one-mode and two-mode behaviors in $Mo_{1-x}W_xS_2$ monolayer alloys, respectively. The broadening of A_1' and WS₂-like E′ modes in the alloys has been observed. The MREI-model was successfully used to predict mode behaviors and fit the composition-dependent Raman frequencies of A_1' and E′ modes. The Raman frequencies of A_1' and E′ modes can be used to quantify Mo/W compositions.

Author contributions

L.X. and Y.H. conceived and designed the experiments. D.D. and Y.H. synthesized $Mo_{1-x}W_xS_2$ single crystals. Y.C., N.M., Q.F. and M.Z. exfoliated $Mo_{1-x}W_xS_2$ samples and performed optical imaging, AFM and Raman characterizations. Y.Z., X.Z. and P.T. performed MREI calculations. Y.C. and L.X. co-wrote the manuscript. J.Z. revised the manuscript. All authors discussed the results and commented on the manuscript.

Acknowledgements

Notes and references

1 D. Haberer, D. Vyalikh, S. Taioli, B. Dora, M. Farjam, J. Fink, D. Marchenko, T. Pichler, K. Ziegler and S. Simonucci, *Nano Lett.*, 2010, **10**, 3360.

2 B. Dai, L. Fu, Z. Zou, M. Wang, H. Xu, S. Wang and Z. Liu, *Nat. Commun.*, 2011, **2**, 522.

3 N. Liu, L. Fu, B. Dai, K. Yan, X. Liu, R. Zhao, Y. Zhang and Z. Liu, *Nano Lett.*, 2010, **11**, 297.

4 Z. H. Ni, T. Yu, Y. H. Lu, Y. Y. Wang, Y. P. Feng and Z. X. Shen, *ACS Nano*, 2008, **2**, 2301.

5 X. Huang, X. Qi, F. Boey and H. Zhang, *Chem. Soc. Rev.*, 2012, **41**, 666.

6 X. Huang, Z. Yin, S. Wu, X. Qi, Q. He, Q. Zhang, Q. Yan, F. Boey and H. Zhang, *Small*, 2011, **7**, 1876.

7 Q. He, S. Wu, Z. Yin and H. Zhang, *Chem. Sci.*, 2012, **3**, 1764.

8 Y. Zhou, X. Jiang, G. Duan, F. Gao and X. T. Zu, *Chem. Phys. Lett.*, 2010, **491**, 203.

9 X. Wang, H. Feng, Y. Wu and L. Jiao, *J. Am. Chem. Soc.*, 2013, **135**, 5304.

10 H. Ramakrishna Matte, A. Gomathi, A. K. Manna, D. J. Late, R. Datta, S. K. Pati and C. Rao, *Angew. Chem., Int. Ed.*, 2010, **122**, 4153.

11 A. Splendiani, L. Sun, Y. Zhang, T. Li, J. Kim, C.-Y. Chim, G. Galli and F. Wang, *Nano Lett.*, 2010, **10**, 1271.

12 X. Huang, Z. Zeng and H. Zhang, *Chem. Soc. Rev.*, 2013, **42**, 1934.

13 H. Li, Z. Yin, Q. He, H. Li, X. Huang, G. Lu, D. W. H. Fam, A. I. Y. Tok, Q. Zhang and H. Zhang, *Small*, 2012, **8**, 63.

14 Z. Zeng, Z. Yin, X. Huang, H. Li, Q. He, G. Lu, F. Boey and H. Zhang, *Angew. Chem., Int. Ed.*, 2011, **50**, 11093.

15 Q. H. Wang, K. Kalantar-Zadeh, A. Kis, J. N. Coleman and M. S. Strano, *Nat. Nanotechnol.*, 2012, **7**, 699.

16 M. Chhowalla, H. S. Shin, G. Eda, L.-J. Li, K. P. Loh and H. Zhang, *Nat. Chem.*, 2013, **5**, 263.

17 W. S. Yun, S. Han, S. C. Hong, I. G. Kim and J. Lee, *Phys. Rev. B: Condens. Matter Mater. Phys.*, 2012, **85**, 033305.

18 A. Kumar and P. Ahluwalia, *Eur. Phys. J. B*, 2012, **85**, 1.

19 Y. Yoon, K. Ganapathi and S. Salahuddin, *Nano Lett.*, 2011, **11**, 3768.

20 Z. Yin, H. Li, H. Li, L. Jiang, Y. Shi, Y. Sun, G. Lu, Q. Zhang, X. Chen and H. Zhang, *ACS Nano*, 2012, **6**, 74.

21 B. Radisavljevic, A. Radenovic, J. Brivio, V. Giacometti and A. Kis, *Nat. Nanotechnol.*, 2011, **6**, 147.

22 J. Liu, Z. Zeng, X. Cao, G. Lu, L. H. Wang, Q. L. Fan, W. Huang and H. Zhang, *Small*, 2012, **8**, 3517.

23 N. Kharche and S. K. Nayak, *Nano Lett.*, 2011, **11**, 5274.

24 W. Zhu, D. Neumayer, V. Perebeinos and P. Avouris, *Nano Lett.*, 2010, **10**, 3572.

25 R. Balog, B. Jørgensen, L. Nilsson, M. Andersen, E. Rienks, M. Bianchi, M. Fanetti, E. Lægsgaard, A. Baraldi and S. Lizzit, *Nat. Mater.*, 2010, **9**, 315.

26 A. Bhattacharya, S. Bhattacharya and G. Das, *Phys. Rev. B: Condens. Matter Mater. Phys.*, 2012, **85**, 035415.

27 R. Zhao, J. Wang, M. Yang, Z. Liu and Z. Liu, *Phys. Chem. Chem. Phys.*, 2013, **15**, 803.

28 H.-P. Komsa and A. V. Krasheninnikov, *J. Phys. Chem. Lett.*, 2012, **3**, 3652.

29 J. Kang, S. Tongay, J. Li and J. Wu, *J. Appl. Phys.*, 2013, **113**, 143703.

30 Y. Chen, J. Xi, D. O. Dumcenco, Z. Liu, K. Suenaga, D. Wang, Z. Shuai, Y.-S. Huang and L. Xie, *ACS Nano*, 2013, **7**, 4610.

31 D. O. Dumcenco, H. Kobayashi, Z. Liu, Y.-S. Huang and K. Suenaga, *Nat. Commun.*, 2013, **4**, 1351.

32 C. Ramkumar, K. Jain and S. Abbi, *Phys. Rev. B: Condens. Matter Mater. Phys.*, 1996, **54**, 7921.

33 V. Y. Davydov, I. Goncharuk, A. Smirnov, A. Nikolaev, W. Lundin, A. Usikov, A. Klochikhin, J. Aderhold, J. Graul and O. Semchinova, *Phys. Rev. B: Condens. Matter Mater. Phys.*, 2002, **65**, 125203.

34 J. Ye, K. Teoh, X. Sun, G. Lo, D. Kwong, H. Zhao, S. Gu, R. Zhang, Y. Zheng and S. Oh, *Appl. Phys. Lett.*, 2007, **91**, 091901.

35 A. Ferrari, J. Meyer, V. Scardaci, C. Casiraghi, M. Lazzeri, F. Mauri, S. Piscanec, D. Jiang, K. Novoselov and S. Roth, *Phys. Rev. Lett.*, 2006, **97**, 187401.

36 A. C. Ferrari, *Solid State Commun.*, 2007, **143**, 47.

37 A. C. Ferrari and D. M. Basko, *Nat. Nanotechnol.*, 2013, **8**, 235.

38 L. Malard, M. Pimenta, G. Dresselhaus and M. Dresselhaus, *Phys. Rep.*, 2009, **473**, 51.

39 Y. Zhao, X. Luo, H. Li, J. Zhang, P. T. Araujo, C. K. Gan, J. Wu, H. Zhang, S. Y. Quek and M. S. Dresselhaus, *Nano Lett.*, 2013, **13**, 1007.

40 X. Zhang, W. Han, J. Wu, S. Milana, Y. Lu, Q. Li, A. Ferrari and P. Tan, *Phys. Rev. B: Condens. Matter Mater. Phys.*, 2012, **87**, 115413.

41 C. Lee, H. Yan, L. E. Brus, T. F. Heinz, J. Hone and S. Ryu, *ACS Nano*, 2010, **4**, 2695.

42 K. F. Mak, C. Lee, J. Hone, J. Shan and T. F. Heinz, *Phys. Rev. Lett.*, 2010, **105**, 136805.

43 B. Chakraborty, H. Matte, A. Sood and C. Rao, *J. Raman Spectrosc.*, 2013, **44**, 92.

44 A. Berkdemir, H. R. Gutiérrez, A. R. Botello-Méndez, N. Perea-López, A. L. Elías, C.-I. Chia, B. Wang, V. H. Crespi, F. López-Urías and J.-C. Charlier, *Sci. Rep.*, 2013, **3**, 1755.

45 C. Sourisseau, M. Fouassier, M. Alba, A. Ghorayeb and O. Gorochov, *Mater. Sci. Eng., B*, 1989, **3**, 119.

46 W. Zhao, Z. Ghorannevis, L. Chu, M. Toh, C. Kloc, P. Tan and G. Eda, *ACS Nano*, 2012, **7**, 791.

47 W. Zhao, Z. Ghorannevis, A. K. Kumar, J. R. Pang, M. Toh, X. Zhang, C. Kloc, P. H. Tan and G. Eda, *Nanoscale*, 2013, **5**, 9677.

48 D. O. Dumcenco, Y.-C. Su, Y.-P. Wang, K.-Y. Chen, Y.-S. Huang, C.-H. Ho and K.-K. Tiong, *Chin. J. Phys.*, 2011, **49**, 270.

49 D. Dumcenco, K. Chen, Y. Wang, Y. Huang and K. Tiong, *J. Alloys Compd.*, 2010, **506**, 940.

50 T. C. Damen, S. Porto and B. Tell, *Phys. Rev.*, 1966, **142**, 570.

51 N. Wakabayashi, H. Smith and R. Nicklow, *Phys. Rev. B: Condens. Matter Mater. Phys.*, 1975, **12**, 659.

52 W. Schutte, J. De Boer and F. Jellinek, *J. Solid State Chem.*, 1987, **70**, 207.

53 A. Molina-Sánchez and L. Wirtz, *Phys. Rev. B: Condens. Matter Mater. Phys.*, 2011, **84**, 155413.

54 H. R. Gutiérrez, N. Perea-López, A. L. Elías, A. Berkdemir, B. Wang, R. Lv, F. López-Urías, V. H. Crespi, H. Terrones and M. Terrones, *Nano Lett.*, 2012, **13**, 3447.

55 H. Li, Q. Zhang, C. C. R. Yap, B. K. Tay, T. H. T. Edwin, A. Olivier and D. Baillargeat, *Adv. Funct. Mater.*, 2012, **22**, 1385.

56 R. Loudon, *Adv. Phys.*, 1964, **13**, 423.

57 G. Frey, R. Tenne, M. Matthews, M. Dresselhaus and G. Dresselhaus, *J. Mater. Res.*, 1998, **13**, 2412.

58 S. Ould Saad Hamady, N. Dupuis, J. Décobert and A. Ougazzaden, *J. Cryst. Growth*, 2008, **310**, 4741.

59 Y.-S. Chen, W. Shockley and G. Pearson, *Phys. Rev.*, 1966, **151**, 648.

60 A. Garg, *Phys. B*, 2006, **383**, 188.

61 I. Chang and S. Mitra, *Phys. Rev.*, 1968, **172**, 924.